

See discussions, stats, and author profiles for this publication at: <https://www.researchgate.net/publication/277056745>

A high-order finite deformation phase-field approach to fracture

Article in *Continuum Mechanics and Thermodynamics* · May 2015

DOI: 10.1007/s00161-015-0440-7

CITATIONS

7

READS

164

2 authors:



[Christian Hesch](#)

Universität Siegen

50 PUBLICATIONS 398 CITATIONS

[SEE PROFILE](#)



[Kerstin Weinberg](#)

Universität Siegen

81 PUBLICATIONS 432 CITATIONS

[SEE PROFILE](#)

Some of the authors of this publication are also working on these related projects:



Electro Active Biological tissues [View project](#)

ORIGINAL ARTICLE

Kerstin Weinberg  · Christian Hesch

A high-order finite deformation phase-field approach to fracture

Received: 7 November 2014 / Accepted: 5 May 2015
© Springer-Verlag Berlin Heidelberg 2015

Abstract Phase-field approaches to fracture allow for convenient and efficient simulation of complex fracture pattern. In this paper, two variational formulations of phase-field fracture, a common second-order model and a new fourth-order model, are combined with a finite deformation ansatz for general nonlinear materials. The material model is based on a multiplicative decomposition of the principal stretches in a tensile and a compressive part. The excellent performance of the new approach is illustrated in classical numerical examples.

Keywords Finite deformations · High-order phase-field model · Isogeometric analysis · Fracture mechanics

1 Introduction

In a phase-field approach to fracture, the crack propagation is described with an additional order parameter—the phase field φ —which marks the intact and the fractured regions of the material. The evolution of the phase field follows an own partial differential equation. The ability of such multi-field methods to simulate cracks growth and sophisticated fracture pattern has been shown in several applications, see, among many others Karma et al. [11], Henry et al. [9], Kuhn and Müller [12], Miehe et al. [14] and Borden et al. [4].

More recently, the employed phase-field approaches to fracture are formulated in an energy-optimizing setting. Such variational formulations for brittle fracture have been introduced and analyzed, e.g., by Ambrosio and Tortorelli [2], Francfort and Marigo [8] and Bourdin et al. [5]. They rely on the minimization of a global energy functional and thus allow for simple finite element discretizations, which lead to accurate and robust numerical approximations. Also in its variational form, the main idea of a phase-field approach to fracture remains to replace the sharp boundary of a crack by a ‘smeared’ crack zone and to describe its evolution by means of a continuous field.

Here, we combine a novel framework for general nonlinear hyperelastic materials with two different variational phase-field approaches. Aside of the second-order form presented in [4, 5, 14], we investigate a potential, which is deduced from a fourth-order partial differential equation. This combination is expected to lead to a sophisticated model, which improves the accuracy and the convergence of the numerical solution in finite elasticity. In order to solve the problem numerically, an isogeometric finite element method is used for

Communicated by Ralf Müller.

K. Weinberg (✉)
Chair of Solid Mechanics, Institute of Mechanics and Control, University of Siegen, Paul-Bonatz-Straße 9-11,
57068 Siegen, Germany
E-mail: kerstin.weinberg@uni-siegen.de

C. Hesch
Institute of Mechanics, Karlsruhe Institute of Technology (KIT), Otto-Ammann-Platz 9, 76131 Karlsruhe, Germany
E-mail: christian.hesch@kit.edu

the spatial discretization of both models. This framework minimizes the numerical and computational effort without sacrificing the required smoothness.

The remaining of the paper is organized as follows: In Sect. 2, the fundamental equations of the mechanical field in the context of nonlinear elasticity are presented. A short discussion of the second- and the fourth-order phase-field model follows in Sect. 2.2. The numerical framework for the solution of the coupled multi-field problem is dealt with in Sect. 2.3. Numerical investigations are presented in Sect. 3, and conclusions are drawn in Sect. 4.

2 Governing equations of phase-field models

In this section, we summarize the variational formulation of the multi-field problem and introduce a general nonlinear framework for the underlying mechanical field. In particular, we consider a Lipschitz bounded domain in its reference configuration $\mathcal{B}_0 \subset \mathbb{R}^d$, $d \in [2, 3]$ for the time interval $t \in \mathcal{I} = [0, T]$. The deformation mapping

$$\boldsymbol{\varphi}(\mathbf{X}, t) : \mathcal{B}_0 \times \mathcal{I} \rightarrow \mathbb{R}^d, \quad (1)$$

characterizes the motion together with a phase field

$$\mathfrak{s}(\mathbf{X}, t) : \mathcal{B}_0 \times \mathcal{I} \rightarrow \mathbb{R}. \quad (2)$$

Here, $\mathbf{X} \in \mathcal{B}_0$ labels material points in the reference configuration, and both fields are assumed to be sufficiently smooth. Additionally, we assume for the phase field $\mathfrak{s} \in [0, 1]$, where a value of $\mathfrak{s} = 0$ refers to the undamaged material and $\mathfrak{s} = 1$ to the ‘cracked zones.’

2.1 Finite strain elasticity in a phase-field approach

Let a Helmholtz free energy density $\Psi : \mathcal{B}_0 \times \mathcal{I} \rightarrow \mathbb{R}$ be given as a function of the right Cauchy–Green tensor $\mathbf{C} = \mathbf{F}^T \mathbf{F}$, where $\mathbf{F} : \mathcal{B}_0 \times \mathcal{I} \rightarrow \mathbb{R}^{d \times d}$ is the deformation gradient and \mathfrak{s} the phase field.

From the physics of the underlying problem, we deduce that fracture requires a local state of tension, whereas the compressive part of the deformation does not contribute to crack growth. Therefore, we define the fracture insensitive part of the deformation gradient as

$$\mathbf{F}^i = \sum_{a=1}^d (\lambda_a^+)^{(1-\mathfrak{s})} \lambda_a^- \mathbf{n}_a \otimes \mathbf{N}_a, \quad (3)$$

where \mathbf{n}_a and \mathbf{N}_a , $a \in [1, \dots, d]$, denote the principal directions of the left and right stretch tensors, respectively. The principal stretches λ_a are decomposed into tensile λ_a^+ and compressive components λ_a^- via $\lambda_a = \lambda_a^+ \lambda_a^-$ with

$$\lambda_a^\pm = [(\lambda_a - 1) \pm |\lambda_a - 1|]/2 + 1. \quad (4)$$

In the following, we abbreviate $\lambda_a^i = (\lambda_a^+)^{(1-\mathfrak{s})} \lambda_a^-$ for the ease of exposition. Accordingly, the Helmholtz free energy density can be defined as $\Psi := \Psi(\mathbf{F}^i, \mathfrak{s})$ or $\Psi := \Psi(\lambda_a, \mathfrak{s}) = \Psi(\lambda_a^i)$.

The first Piola–Kirchhoff stress tensor follows as

$$\mathbf{P} = \frac{\partial \Psi}{\partial \mathbf{F}} = \sum_{a=1}^d \frac{\partial \Psi}{\partial \lambda_a^i} \frac{\partial \lambda_a^i}{\partial \lambda_a} \mathbf{n}_a \otimes \mathbf{N}_a = \sum_{a=1}^d P_a \mathbf{n}_a \otimes \mathbf{N}_a, \quad (5)$$

whereas the second Piola–Kirchhoff stress tensor reads

$$\mathbf{S} = 2 \frac{\partial \Psi}{\partial \mathbf{C}} = \sum_{a=1}^d \frac{1}{\lambda_a} P_a \mathbf{N}_a \otimes \mathbf{N}_a. \quad (6)$$

Introducing the local balance of linear momentum $\nabla_{\mathbf{X}} \cdot \mathbf{P} + \bar{\mathbf{B}} = \rho_0 \dot{\mathbf{v}}$ with prescribed body forces $\bar{\mathbf{B}}$, mass density ρ_0 and material velocity \mathbf{v} , we obtain the weak form of the mechanical problem

$$\begin{aligned} & \int_{\mathcal{B}_0} \delta \boldsymbol{\varphi} \cdot \rho_0 \dot{\mathbf{v}} \, dV + \int_{\mathcal{B}_0} \mathbf{S} : (\mathbf{F})^T \nabla_{\mathbf{X}} (\delta \boldsymbol{\varphi}) \, dV \\ &= \int_{\mathcal{B}_0} \delta \boldsymbol{\varphi} \cdot \bar{\mathbf{B}} \, dV + \int_{\partial \mathcal{B}_0^g} \delta \boldsymbol{\varphi} \cdot \bar{\mathbf{T}} \, dA, \quad \forall \delta \boldsymbol{\varphi} \in \mathcal{V}^\varphi. \end{aligned} \quad (7)$$

Here, the functional space of admissible test functions $\delta \boldsymbol{\varphi}$ is introduced as

$$\mathcal{V}^\varphi = \{\delta \boldsymbol{\varphi} \in \mathcal{H}^1(\mathcal{B}_0) | \delta \boldsymbol{\varphi} = \mathbf{0} \text{ on } \partial \mathcal{B}_0^\varphi\}, \quad (8)$$

where \mathcal{H}^1 denotes the Sobolev functional space of square integrable functions with square integrable weak derivative. Moreover, the terms on the right-hand side of Eq. (7) represent the external contributions, where we have made use of the classical Dirichlet and Neumann boundary conditions

$$\boldsymbol{\varphi} = \bar{\boldsymbol{\varphi}} \text{ on } \partial \mathcal{B}_0^\varphi \times \mathcal{I} \quad \text{and} \quad \mathbf{P}\mathbf{N} = \bar{\mathbf{T}} \text{ on } \partial \mathcal{B}_0^g \times \mathcal{I}, \quad (9)$$

as well as of the initial conditions

$$\boldsymbol{\varphi}(\mathbf{X}, 0) = \mathbf{X}_0 \quad \text{and} \quad \mathbf{v}(\mathbf{X}, 0) = \mathbf{v}_0 \text{ in } \mathcal{B}_0. \quad (10)$$

2.2 Phase-field theory

The evolution of a phase-field introduced in Eq. (2) is typically described by a partial differential equation, which may be, e.g., of the Allen–Cahn type,

$$\dot{u} = c_2 \Delta u - c_1(u - u^3), \quad (11)$$

here formulated for an arbitrary field¹ $u(\mathbf{x}, t)$ and constants c_1, c_2 . The convective term Δu describes the diffusion of field u , whereas the reaction term $c_1(u - u^3)$ works as a driving force, i.e., a variation of some energy function. To be specific, such a free energy density

$$\psi_1 = c_1 \frac{1}{4} (1 - u^2)^2 \Rightarrow \delta_u \psi_1 = c_1(u^3 - u) \quad (12)$$

has a double well shape with two minima and is shown in Fig. 1. Analogously, the diffusion term can be deduced from an energy density,

$$\psi_2 = c_2 \frac{1}{2} |\nabla u|^2 \Rightarrow \delta_u \psi_2 = -c_2 \Delta u, \quad (13)$$

and with $\psi = \psi_2 + \psi_1$ the Allen–Cahn Eq. (11) can alternatively be written as

$$\dot{u} = -\delta_u \left[c_2 \frac{1}{2} |\nabla u|^2 + c_1 \frac{1}{4} (1 - u^2)^2 \right]. \quad (14)$$

For simplification, a linearized version the Allen–Cahn equation may be introduced as follows

$$\dot{u} = c_2 \Delta u - c_0(1 - u), \quad (15)$$

and we obtain for the free energy function of the reaction term

$$\psi_0 = c_0 \frac{1}{2} (1 - u)^2 \Rightarrow \delta_u \psi_0 = -c_0(1 - u). \quad (16)$$

Again, this equation can be written similar to (14) with $\psi = \psi_2 + \psi_0$ as

$$\dot{u} = -\delta_u \left[c_2 \frac{1}{2} |\nabla u|^2 + c_0 \frac{1}{2} (1 - u)^2 \right]. \quad (17)$$

¹ We follow here the usual phase-field convention and define $u(\mathbf{x}, t)$ in such a way that it reduces as a consequence of dissipation. Compared to our phase-field approach to fracture, this corresponds to $u = 1 - \mathfrak{s}$.

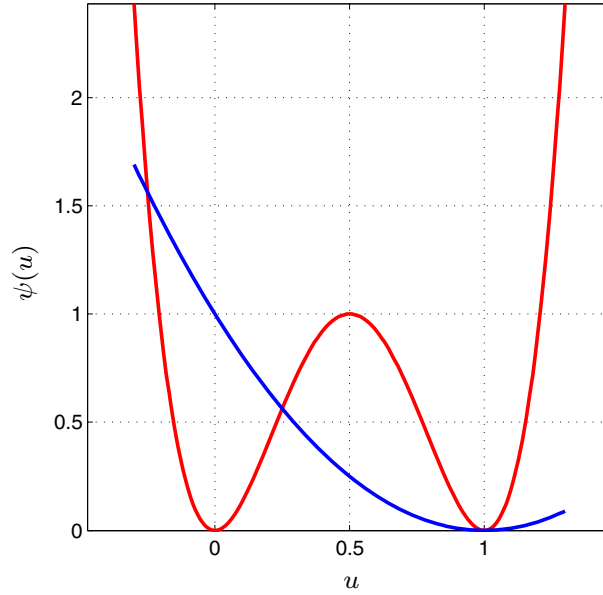


Fig. 1 Classical double well functional with two minima and simplified quadratic energy functional employed for phase-field fracture

A different reaction–diffusion equation is the Cahn–Hilliard equation

$$\dot{u} = c_4 \Delta \Delta u + c_3 u, \quad (18)$$

which is of fourth order. Using the same formalism as above and with $c_4 = -c_2$ and $c_3 = 6c_1$ in (13) and (12), it can be reformulated as $\dot{u} = -\nabla \cdot \nabla \delta_u (\psi_2 + \psi_1)$, which shows the typical structure of a continuity equation. However, in phase-field fracture neither the ‘cracked zone size’ nor the elastic strain energy is a preserved quantity, and thus, a direct application of Eq. (18) is not meaningful. Nevertheless, the bilaplacian term $\Delta \Delta u$ enforces a steep transition from one phase to the other and may sharpen a diffuse interface approximation of the crack boundary.

As before, a variational formulation can be derived using

$$\psi_4 = c_4 \frac{1}{2} (\Delta u)^2 \Rightarrow \delta_u \psi_4 = c_4 \Delta \Delta u, \quad (19)$$

and we obtain a fourth-order differential equation for phase-field evolution

$$\dot{u} = -c_4 \Delta \Delta u + c_2 \Delta u + c_0 (1 - u), \quad (20)$$

with corresponding energy functional $\psi = \psi_4 + \psi_2 + \psi_0$ such that

$$\dot{u} = -\delta_u \left[c_4 \frac{1}{2} (\Delta u)^2 + c_2 \frac{1}{2} |\nabla u|^2 + c_0 \frac{1}{2} (1 - u)^2 \right]. \quad (21)$$

Note that there is no natural choice of differential equation for phase-field fracture modeling. Several authors use directly the Allen–Cahn Eq. (11), see, e.g., Karma et al. [11], Henry et al. [9], others prefer the linearized Allen–Cahn Eq. (15). Its variational form leads directly to the popular ansatz of Bourdin [5] which is employed, e.g., in Kuhn and Müller [12], Miehe et al. [14] and Abdollahi and Arias [1]. Borden et al. [3] recently introduced a phase-field ansatz corresponding to the fourth-order equation (20). The formulation of other reaction–diffusion equations with higher derivatives is possible and only constrained by objectivity and invariance to coordinate transformations, see Lai and Sarma [13] for a related discussion.

Additionally, the choice of the parameters $c_0 \dots c_4$ is up to modeling. Here, they are defined such that all gradients are weighted in the same way and introduce an ‘intrinsic crack width’ or length l . According to fracture mechanics, a material fails upon attainment of a critical fracture energy density g_c . Therefore, all terms in the free energy functional have sum up to material parameter g_c times the crack surface.

Crack growth stands for the creation of new boundaries $\Gamma(t) \subset \mathbb{R}^{n-1}$, and hence, the total potential energy of a body is composed of its elastic energy contribution and a crack functional with evolving boundaries:

$$E(\varphi) = \int_{B_0} \Psi(\varphi) dV + \int_{\Gamma_0(t)} g_c d\Gamma. \quad (22)$$

Since such an energy functional cannot be optimized in general, in a variational approach to fracture the set of evolving crack boundaries is replaced by a crack-density functional $\gamma(t) =: \gamma(\mathfrak{s}(t))$ with $\int_{\Gamma_0(t)} d\Gamma \approx \int_{B_0} \gamma(t) dV$. Then, the total potential energy of the body reads

$$E(\mathbf{C}, \mathfrak{s}) = \int_{B_0} \Psi(\mathbf{C}, \mathfrak{s}) dV + \int_{B_0} g_c \gamma(\mathfrak{s}) dV. \quad (23)$$

A specific choice of the elastic strain energy density $\Psi(\mathbf{C}, \mathfrak{s})$ will be given in Sect. 3.

In order to specify the crack-density functional, we consider the free energy density (17), which corresponds to the second-order partial differential equation (15). For constants $c_0 = g_c/4l$ and $c_2 = g_cl$, it follows directly the functional of Bourdin [5]. With slightly modified parameters $c_0 = g_c/2l$ and $c_2 = g_cl/2$, we define the crack-density functional as

$$\gamma(\mathfrak{s}) = \frac{1}{2l} \mathfrak{s}^2 + \frac{l}{2} |\nabla \mathfrak{s}|^2 \quad (24)$$

which will subsequently be referred to as second-order model. The free energy density (21) corresponding to Eq. (20) and specified with constants $c_0 = g_c/4l$, $c_2 = g_cl/2$, $c_4 = g_cl^3/4$ results in the crack-density functional

$$\gamma(\mathfrak{s}) = \frac{1}{4l} \mathfrak{s}^2 + \frac{l}{2} \nabla(\mathfrak{s}) \cdot \nabla(\mathfrak{s}) + \frac{l^3}{4} \Delta^2(\mathfrak{s}) \quad (25)$$

which will be referred to as fourth-order model.

The weak form of the second-order phase-field approach in Eq. (24) follows immediately by taking the variation of the total potential energy (23) with respect to \mathfrak{s}

$$\int_{B_0} \delta \mathfrak{s} \left(\frac{g_c}{l} \mathfrak{s} + \frac{\partial \Psi(\mathbf{C}, \mathfrak{s})}{\partial \mathfrak{s}} \right) + g_cl \nabla(\delta \mathfrak{s}) \cdot \nabla(\mathfrak{s}) dV = 0 \quad \forall \delta \mathfrak{s} \in \mathcal{V}_1^\mathfrak{s}, \quad (26)$$

where the functional space of admissible test functions of the second-order phase field is introduced as

$$\mathcal{V}_1^\mathfrak{s} = \{\delta \mathfrak{s} \in \mathcal{H}^1(B_0) | \delta \mathfrak{s} = 0 \text{ on } \Gamma(t)\}. \quad (27)$$

The corresponding weak form of the fourth-order phase-field approach in Eq. (25) reads

$$\int_{B_0} \delta \mathfrak{s} \left(\frac{g_c}{2l} \mathfrak{s} + \frac{\partial \Psi(\mathbf{C}, \mathfrak{s})}{\partial \mathfrak{s}} \right) + g_cl \nabla(\delta \mathfrak{s}) \cdot \nabla(\mathfrak{s}) + \frac{g_cl^3}{2} \Delta(\delta \mathfrak{s}) \Delta(\mathfrak{s}) dV = 0 \quad \forall \delta \mathfrak{s} \in \mathcal{V}_2^\mathfrak{s}, \quad (28)$$

with functional space of admissible test functions

$$\mathcal{V}_2^\mathfrak{s} = \{\delta \mathfrak{s} \in \mathcal{H}^2(B_0) | \delta \mathfrak{s} = 0 \text{ on } \Gamma(t)\}, \quad (29)$$

which requires—in contrast to the requirements of the second-order phase-field approach (26)—the Sobolev space $\mathcal{H}^2(B_0)$. Boundary conditions are given by $\nabla \mathfrak{s} \cdot \mathbf{n} = 0$ on ∂B_0 , $\Delta \mathfrak{s} = 0$ on ∂B_0 . Moreover, initial conditions are $\mathfrak{s}(\mathbf{X}, 0) = 0$ on B_0 , describing an unbroken initial state. This completes the set of equations for the initial coupled phase-mechanical boundary value problem.

Remark Note that the weak forms in Eqs. (26), (28) and (7) are derived consistently from specific forms of energy (23). The coupling between deformation and phase field follows immediately from this variational structure.

2.3 Numerical approximation

In order to perform the spatial discretization for the numerical solution of the problem, the domain \mathcal{B}_0 in the reference configuration is subdivided into a finite set of non-overlapping elements $e \in \mathcal{E}$

$$\mathcal{B}_0 \approx \mathcal{B}_0^h = \bigcup_e \mathcal{B}_{0,e}, \quad \forall e \in \mathcal{E}. \quad (30)$$

We introduce finite dimensional approximations of the deformation field and its variation

$$\boldsymbol{\varphi}^h = \sum_{A \in \omega} R^A \mathbf{q}_A, \quad \delta \boldsymbol{\varphi}^h = \sum_{A \in \omega} R^A \delta \mathbf{q}_A, \quad (31)$$

and of the phase field and its variation

$$\mathfrak{s}^h = \sum_{A \in \omega} R^A \mathfrak{s}_A, \quad \delta \mathfrak{s}^h = \sum_{A \in \omega} R^A \delta \mathfrak{s}_A. \quad (32)$$

Note that we use a conform mesh for both fields, where $A \in \omega = \{1, \dots, n_{\text{node}}\}$ and $R^A(\mathbf{X}) : \mathcal{B}_0 \rightarrow \mathbb{R}$ are global shape functions.

The required continuity $\mathfrak{s}^h \in \mathcal{V}^s \subset \mathcal{H}^2(\mathcal{B}_0)$ can be fulfilled by piecewise smooth basis functions R^A , which are globally at least C^1 continuous. Other approaches, like mixed finite element formulations or discrete Galerkin methods, are possible but will not be pursued. In this work, we apply rational B-splines as finite element basis functions for both fields, given as follows

$$R^A = R_{p,q,r}^{i,j,\mathfrak{k}}(\boldsymbol{\xi}) = \frac{N_{i,p}(\boldsymbol{\xi}) M_{j,q}(\boldsymbol{\eta}) L_{\mathfrak{k},r}(\boldsymbol{\zeta}) w_{i,j,\mathfrak{k}}}{\sum_{\hat{i}=1}^n \sum_{\hat{j}=1}^m \sum_{\hat{\mathfrak{k}}=1}^l N_{\hat{i},p}(\boldsymbol{\xi}) M_{\hat{j},q}(\boldsymbol{\eta}) L_{\hat{\mathfrak{k}},r}(\boldsymbol{\zeta}) w_{\hat{i},\hat{j},\hat{\mathfrak{k}}}}. \quad (33)$$

Here, n, m, l denote the number of control points along each parametric direction. In addition, p, q, r denote the order of the non-rational B-Splines N, M and L , recursively defined as follows

$$N_{i,p} = \frac{\xi - \xi_i}{\xi_{i+p} - \xi_i} N_{i,p-1}(\xi) + \frac{\xi_{i+p+1} - \xi}{\xi_{i+p+1} - \xi_{i+1}} N_{i+1,p-1}(\xi), \quad (34)$$

beginning with

$$N_{i,0}(\xi) = \begin{cases} 1 & \text{if } \xi_i \leq \xi < \xi_{i+1}, \\ 0 & \text{otherwise.} \end{cases} \quad (35)$$

The definition for M and L follows analogously. Due to this specific construction, rational B-spline functions allows to predefine the continuity, such that we obtain higher-order accuracy, robustness, and, most importantly, C^1 continuity if necessary. For more details of the NURBS construction, in particular for the choice of the NURBS weights $w_{i,j,\mathfrak{k}}$, we refer to Piegel and Tiller [15]. The shape functions are associated with a net of control points \mathbf{q}_A , such that a geometrical map $\mathfrak{F} : \hat{\mathcal{B}}_0 \rightarrow \mathcal{B}_0$, where $\hat{\mathcal{B}}_0$ represents the index space, can be defined to link the parameter and the physical space, cf. da Veiga et al. [7] and Brivadis et al. [6]

$$\boldsymbol{\varphi}^h := \mathfrak{F}(\boldsymbol{\xi}) = R_{p,q,r}^{i,j,\mathfrak{k}}(\boldsymbol{\xi}) \mathbf{q}_{i,j,\mathfrak{k}}. \quad (36)$$

The finite element mesh is now determined via knot vectors, which subdivide the parameter space into elements.

Next, we discretize the system in time by considering a sequence of times $t_0, \dots, t_n, t_{n+1}, \dots, T$, where $(\bullet)_n$ and $(\bullet)_{n+1}$ denote the value of a given physical quantity at time t_n and t_{n+1} , respectively. Additionally, the time-step size is given by $\Delta t = t_{n+1} - t_n$ and $t_{n+1/2} = 0.5(t_{n+1} + t_n)$ denote the usual midpoint approximation. The full discrete set of equations of the coupled multi-field system follows directly by inserting ansatz (31–33) into the weak forms (7) and (26) or (28). We refer to the latter,

$$\begin{aligned} \delta \mathbf{q}_A \cdot \left[M^{AB} \frac{\mathbf{v}_{B,n+1} - \mathbf{v}_{B,n}}{\Delta t} + \int_{\mathcal{B}_0} \nabla R^A \cdot \mathbf{S}_{n,n+1}^{e,h} \nabla R^B \, dV \mathbf{q}_{B,n+1/2} \right] \\ = \delta \mathbf{q}_A \cdot \left[\mathbf{F}_{n+1/2}^{A,ext} \right], \end{aligned} \quad (37)$$

$$\begin{aligned} \delta \mathfrak{s}_A \left[\int_{\mathcal{B}_0} \frac{g_c}{2l} R^A R^B \mathfrak{s}_{B,n+1/2} + g_c l \nabla R^A \cdot \nabla R^B \mathfrak{s}_{B,n+1/2} \right. \\ \left. + \frac{g_c l^3}{2} \Delta R^A \Delta R^B \mathfrak{s}_{B,n+1/2} \, dV \right] = -\delta \mathfrak{s}_A \int_{\mathcal{B}_0} \left(\frac{\partial \Psi}{\partial \mathfrak{s}_A} \right)_{n+1/2} \, dV. \end{aligned} \quad (38)$$

The consistent mass matrix is denoted by M^{AB} , whereas $\mathbf{F}_{n+1/2}^{A,ext}$ represents the nodal external load vector. The algorithmic version of the discretized second Piola–Kirchhoff stress tensor for the construction of a structure preserving temporal discretization scheme is given by

$$\mathbf{S}_{n,n+1}^{e,h} = 2 \frac{\partial \Psi_{n+1/2}}{\partial \mathbf{C}^h} + 2 \frac{\Psi_{n+1} - \Psi_n + g_c(\gamma_{n+1} - \gamma_n) - \frac{\partial \Psi_{n+1/2}}{\partial \mathbf{C}^h} : \Delta \mathbf{C}^h}{\Delta \mathbf{C}^h : \Delta \mathbf{C}^h} \Delta \mathbf{C}^h. \quad (39)$$

The proposed scheme preserves algorithmically both momentum maps as well as total energy of the whole system, see Hesch and Weinberg [10] for a detailed proof.

3 Numerical simulations

For the numerical simulations, a two-dimensional square plate with an initial horizontal notch is considered. The constitutive behavior is assumed to be governed by a hyperelastic compressible neo-Hookean material with elastic strain energy

$$\Psi(\lambda_a^i) = \frac{\mu}{2} \left(\sum_{a=1}^n (\lambda_a^i)^2 - n \right) + \frac{\kappa}{2} (\ln(J))^2 - \mu \ln(J), \quad (40)$$

where $J = \prod_{a=1}^n \lambda_a^i$ and κ, μ denote the Lamé coefficients, where κ is chosen instead of λ to avoid conflicts in notation. In our examples, we set $\kappa = 121.154 \times 10^9 \text{ N/m}^2$ and $\mu = 80.769 \times 10^9 \text{ N/m}^2$. All computations refer to a displacement controlled quasi-static loading regime.

A uniform NURBS mesh with quadratic shape functions has been applied to both, the mechanical and the phase field. In order to embed the horizontal notch within the C^1 continuous field, the rectangular area has been decomposed into two parts. The arising interface enables us to maintain the C^1 continuity across the interface, see Fig. 2 for the partially overlapping control mesh. In order to obtain the prescribed notch, only the right half of the nodes has been constrained.

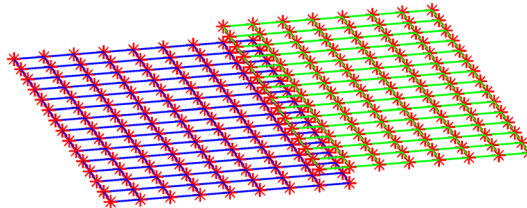


Fig. 2 Overlapping control mesh for C^1 -continuous domain decomposition along the notch

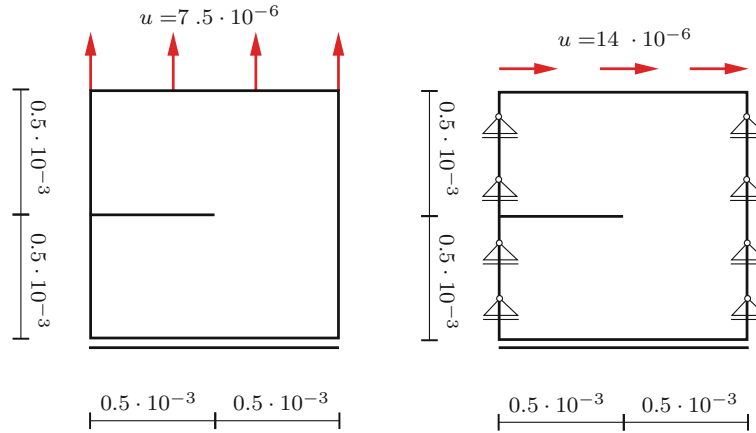


Fig. 3 Geometry and boundary conditions for the example problems: mode I—tension test and mode II—shear test. The units of all values given refer to [m, N, s]

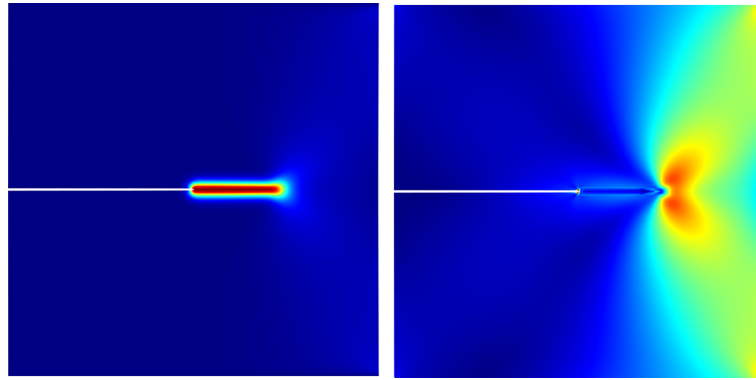


Fig. 4 Single-edge-notched tension test simulated with the fourth-order phase-field ansatz (28) at a prescribed displacement of $u = 6 \times 10^{-6}$ m. On the *left* the phase field is shown (blue: 0, red: 1), and on the *right* the corresponding von Mises stress distribution is displayed (blue: 0, red: maximum) (color figure online)

3.1 Notched tension test

We begin with a symmetric tension test with the specific boundary conditions shown in Fig. 3. The critical energy release rate is chosen to be $g_c = 2700$ N/m, and the fixed length-scale parameter is $l = 7.5 \times 10^{-6}$ m. The load is applied using constant displacement increments $\Delta u = 1 \times 10^{-7}$ m. The uniform mesh consists of 256×256 isogeometric elements, such that $h \approx l/2$. This corresponds to a total of 201,240 degrees of freedom for the mechanical and the phase field. A staggered scheme has been applied to prevent the system from cracking in a single step.

The resulting phase field for the fourth-order phase-field model and the corresponding von Mises stress distribution in the actual configuration are displayed in Fig. 4. The results refer to a prescribed displacement at the upper boundary of $u = 6 \times 10^{-6}$ m. Phase field and stresses look basically the same for the second-order phase-field ansatz (26); only the phase field is slightly smoother, i.e., the crack zone looks more diffuse in the high-order approach. Preliminary results indicate a significant faster convergence of the fourth-order ansatz (28).

Figure 5 shows the load–deflection curves for both, the second-order approach (26) and the fourth-order approach (28). All parameters, i.e., material, length scale and critical energy release rate as well as the mesh using quadratic NURBS shape functions and the applied displacement steps, are exactly identical. Obviously, a higher continuity in the phase field leads in the critical range to a more compliant response. The fourth-order phase-field model (28) better maps the structure’s softening as a result of cracking.

Additionally, the result of Miehe et al. [14] which is obtained with the same Lamé coefficients and loading conditions has been plotted within this figure. To allow for comparison, the prescribed displacement is converted

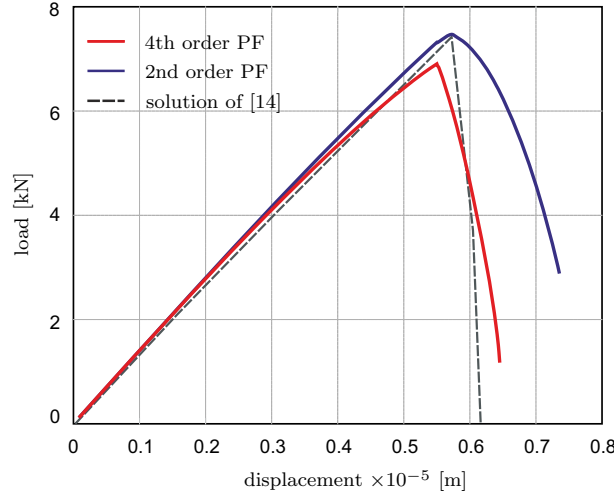


Fig. 5 Single-edge-notched tension test. Load–deflection curves for the fourth-order and the second-order phase-field ansatz and for comparison the linear-elastic solution of Miehe et al. [14]

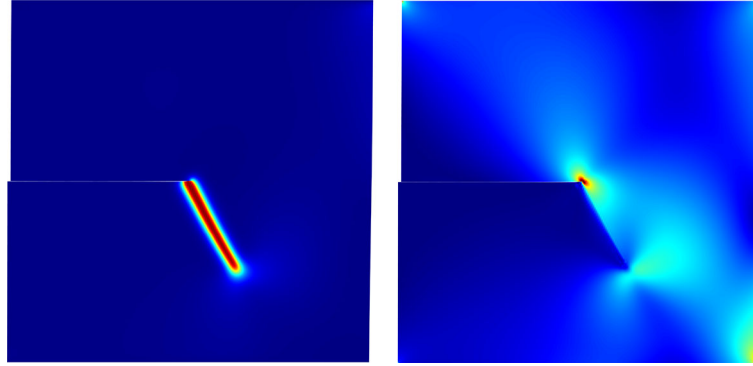


Fig. 6 Single-edge-notched shear test simulated with the fourth-order phase-field ansatz (28) at a prescribed displacement of $u = 1.15 \times 10^{-5}$ m. On the *left* the phase-field is shown (blue: 0, red: 1), and on the *right* the corresponding von Mises stress distribution is displayed (blue: 0, red: maximum) (color figure online)

into a force $F = EAu/l$ assuming a plate thickness of 4.76×10^{-4} m. The linear-elastic solution of [14] bases on a second-order phase-field approach and is solved with a very fine piecewise-linear finite element mesh (30,000 triangles). Up to the limit load, this solution almost coincides with the corresponding NURBS mesh. Softening, however, is mapped much more smoothly with high-order shape functions.

3.2 Notched shear test

In the next example, the same geometry and discretization as before are used, except for the modified boundary conditions, see Fig. 3. The prescribed displacement at the upper boundary now moves horizontally. After the crack is initialized, the prescribed displacement step size is reduced to $\Delta u = 1 \times 10^{-6}$ m for reasons of stability of the Newton iteration. All material properties remain unchanged.

Boundary conditions are applied such that a pure shear deformation follows and the crack propagates in mode II. The resulting phase field as well as the von Mises stress distribution in the actual configuration is shown in Fig. 6. Again, the results for the fourth-order phase-field model (28) are compared to the second-order phase-field model (26) using an otherwise identical model. The corresponding load–deflection curves are plotted in Fig. 7 together with a linear-elastic solution of [4] and [14]. Analogous to the previous example, the numerical simulation of the higher-order model shows a softer behavior of the structure. In particular, the difference to the linear-elastic solution of Borden et al. [4]—obtained with a second-order phase-field

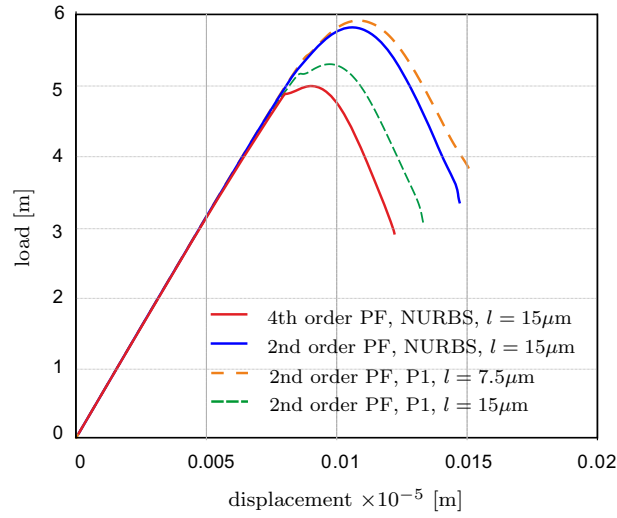


Fig. 7 Single-edge-notched shear test. Load–deflection curves for the fourth-order and the second-order phase-field ansatz and for comparison linear-elastic solutions computed with a second-order phase field and a piecewise-linear Lagrangian mesh with $l = 7.5 \times 10^{-6}$ m corresponding to the solution of Miehe et al. [14], and with $l = 15 \times 10^{-6}$ m, results corresponding to the solution of Borden et al. [4]

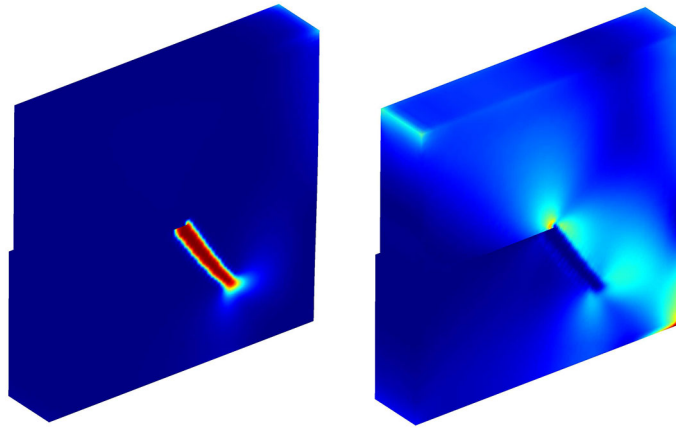


Fig. 8 Distribution of the phase field and the von Mises stress in the single-edge-notched shear test simulated with the fourth-order phase field at a horizontal displacement of $u = 1.1 \times 10^{-5}$ m

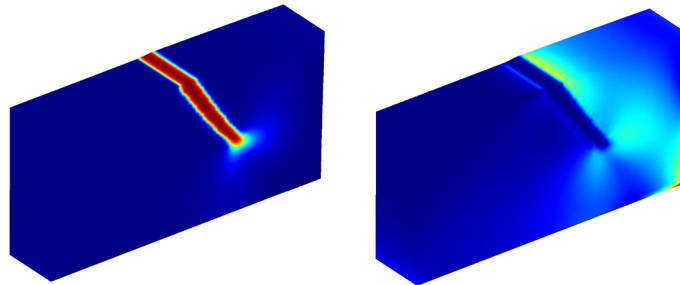


Fig. 9 Distribution of the phase field and the von Mises stress in the single-edge-notched shear test, lower part of the system displayed

ansatz and T-spline-based finite element mesh—can be noticed. This is mainly attributed to a different length parameter l . Additionally, the softening due to crack propagation is captured earlier with the fourth-order phase-field ansatz (28).

3.3 Three-dimensional shear test

Finally, we show the results of a three-dimensional simulation of an edge-notched block. The geometry of the block corresponds to the ones shown in Fig. 3, using a thickness of $1/5 \times 10^{-3}$ m. The material is again assumed to be neo-Hookean with strain energy density (40) and finite deformation split (3).

The upper boundary of the block moves horizontally and induces a shear deformation, which leads to mode II crack growth. In Fig. 8, the computed stress distribution together with the phase field is displayed after 100 time steps. In Fig. 9, the corresponding stress distribution within the block is shown which illustrates the ability of the fourth-order phase-field approach to conveniently simulate crack growth.

4 Conclusions

This paper presents a fourth-order phase-field model along with a general nonlinear framework for finite elasticity in the mechanical field. As a consequence of the higher-order phase-field ansatz requiring C^1 continuity, the use of an isogeometrical framework is beneficial. In particular, quadratic NURBS shape functions are used throughout the numerical investigations, comparing for the first time results for the commonly used second-order phase-field model with a new fourth-order approach.

Due to the higher regularity of the model, the presented approach gives improved results for crack initialization and propagation, as observed in Figs. 5 and 7. Moreover, the chosen multiplicative decomposition of the deformation gradient into a compressive and a tensile part can be used independent of the specific formulation of the strain energy function as well as of the chosen phase-field fracture model. This allows a most flexible application of the phase-field model to general nonlinear material models.

At last, the applicability to three-dimensional problems is demonstrated. The extension of the considered phase-field model is straightforward, although computationally demanding. This necessitates the application of local, adaptive refinement schemes, to be investigated in a follow-up paper.

Acknowledgments Support for this research was provided by the Deutsche Forschungsgemeinschaft (DFG) under Grant WE2525/4-1, HE5943/5-1 and HE5943/6-1. This support was gratefully acknowledged.

References

1. Abdollahi, A., Arias, I.: Phase-field modeling of crack propagation in piezoelectric and ferroelectric materials with different electromechanical crack conditions. *J. Mech. Phys. Solids* **60**(12), 2100–2126 (2012)
2. Ambrosio, L., Tortorelli, V.M.: Approximation of functional depending on jumps by elliptic functional via t -convergence. *Commun. Pure Appl. Math.* **43**(8), 999–1036 (1990)
3. Borden, M.J., Hughes, T.J.R., Landis, C.M., Verhoosel, C.V.: A higher-order phase-field model for brittle fracture: formulation and analysis within the isogeometric analysis framework. *Comput. Methods Appl. Mech. Eng.* **273**, 100–118 (2014)
4. Borden, M.J., Verhoosel, C.V., Scott, M.A., Hughes, T.J.R., Landis, C.M.: A phase-field description of dynamic brittle fracture. *Comput. Methods Appl. Mech. Eng.* **217–220**, 77–95 (2012)
5. Bourdin, B.: The variational formulation of brittle fracture: numerical implementation and extensions. In: volume 5 of IUTAM Symposium on Discretization Methods for Evolving Discontinuities, IUTAM Bookseries, Chap. 22, pp. 381–393. Springer Netherlands (2007)
6. Brivadis, E., Buffa, A., Wohlmuth, B.I., Wunderlich, L.: Isogeometric mortar methods. *Comput. Methods Appl. Mech. Eng.* **284**, 292–319 (2015)
7. da Veiga, L.B., Cho, D., Pavarino, L.F., Scacchi, S.: Overlapping Schwarz methods for isogeometric analysis. *SIAM J. Numer. Anal.* **50**, 1394–1416 (2012)
8. Francfort, G.A., Marigo, J.-J.: Revisiting brittle fracture as an energy minimization problem. *J. Mech. Phys. Solids* **46**, 1319–1342 (1998)
9. Henry, H., Levine, H.: Dynamic instabilities of fracture under biaxial strain using a phase field model. *Phys. Rev. Lett.* **93**, 105505 (2004)
10. Hesch, C., Weinberg, K.: Thermodynamically consistent algorithms for a finite-deformation phase-field approach to fracture. *Int. J. Numer. Methods Eng.* **99**, 906–924 (2014)
11. Karma, A., Kessler, D.A., Levine, H.: Phase-field model of mode III dynamic fracture. *Phys. Rev. Lett.* **81**, 045501 (2001)
12. Kuhn, C., Müller, R.: A continuum phase field model for fracture. *Eng. Fract. Mech.* **77**, 3625–3634 (2010)
13. Lai, Z.-W., Das Sarma, S.: Kinetic growth with surface relaxation: continuum versus atomistic models. *Phys. Rev. Lett.* **66**, 2348–2351 (1991)
14. Miehe, C., Hofacker, M., Welschinger, F.: A phase field model for rate-independent crack propagation: Robust algorithmic implementation based on operator splits. *Comput. Methods Appl. Mech. Eng.* **199**, 2765–2778 (2010)
15. Piegl, L., Tiller, W.: The NURBS Book, 2nd edn. Springer, Berlin, Heidelberg (2010)